TIER: Text-Image Entropy Regularization
for Medical CLIP-style models

Anil Palepu   APALEPU@MIT.EDU
Health Science and Technology
Harvard-MIT
Cambridge, MA, USA

Andrew Beam   ANDREW_BEAM@HMS.HARVARD.EDU
Epidemiology & Biomedical Informatics
Harvard University
Cambridge, MA, USA

Abstract

In this paper, we introduce a novel regularization scheme on contrastive language-image pre-trained (CLIP) medical vision models. Our approach is based on the observation that, for many medical imaging tasks, text tokens should only describe a small number of image regions and, likewise, each image region should correspond to only a few text tokens. In CLIP-style models, this implies that text-token embeddings should have high similarity to only a small number of image-patch embeddings for a given image-text pair. We formalize this observation using a novel regularization scheme that penalizes the entropy of the text-token to image-patch similarity scores. We qualitatively and quantitatively demonstrate that the proposed regularization scheme improves localization by shrinking most of the pairwise text-token and image-patch similarity scores towards zero, thus achieving the desired effect. We demonstrate the promise of our approach in an important medical context, chest x-rays, where this underlying sparsity hypothesis naturally arises. Using our proposed approach, we achieve state of the art (SOTA) average zero-shot performance on the CheXpert and Padchest chest x-ray datasets, outperforming an unregularized version of the model and several recently published self-supervised models.

1. Introduction

Self-supervised vision models that leverage paired text data such as the contrastive language-image pre-trained (CLIP) model (Radford et al., 2021; Zhang et al., 2020) have demonstrated very impressive zero-shot classification performance in a variety of domains (Radford et al., 2021; Tiu et al., 2022; Boecking et al., 2022; Palepu and Beam, 2022). Specifically, users can leverage the unified text and image embedding space for zero-shot classification by providing relevant text queries and assessing image embedding similarities (Radford et al., 2021; Tiu et al., 2022; Kumar et al., 2022). However, these models only align the representations at the level of the entire image and the entire text caption rather than at a more fine-grained level. In many medical imaging settings, it is often the case that specific clinical findings are only present in a small portion of the image or corresponding radiology report. Thus, in these settings, encouraging sparser cross-modality similarities could improve the learned representations and downstream performance of CLIP-style models.

The base CLIP architecture consists of a vision encoder, typically a CNN (He et al., 2016) or vision transformer (Dosovitskiy et al., 2020), and a text encoder, typically a text transformer (Vaswani et al., 2017). Each encoder produces a global embedding in the joint embedding space that aims to summarize all of the relevant information in their respective modality. A recent modification to this CLIP architecture from Boecking et al. (2022), which was built on chest x-ray (CXR) data, allows for a more fine-grained representation of images by projecting the final ResNet block's output to the joint embedding space prior to doing a global average pooling. As a result, this model produces a set of local or *patch* embeddings which can be indicative of not just *if* a text and image align, but also *roughly where* they align. As an example, in a CXR positive for cardiomegaly (an enlarged heart), the patch embeddings near the heart should have a higher cosine similarity to the text embedding of "an enlarged heart" than other regions would.

In this CXR setting, clinical findings are often confined to a small portion of the image (see Tab. 1). For example, cardiomegaly is primarily identified in the lower left portion of the chest, but a CXR captures many regions beyond this area. Similarly, complex image captions can describe several diverse clinical findings which are unlikely to all correspond to the exact same CXR region. In this work, we propose a method to encode these observations into any CLIP-style model that can produce individual image-patch embeddings and text-token embeddings. To do so, we introduce text-image entropy regularization (TIER), which encourages text-token embeddings and image-patch embeddings to be less 'promiscuous' by regularizing the entropy of a softmaxed distribution of similarity scores. This regularization can be modulated by adjusting two hyperparameters, and because it is based on entropy, it is robust to positional shifts in both the text and the images.

We implement our TIER method leveraging the pre-trained architecture from Boecking et al. (2022), and demonstrate both qualitatively and quantitatively that our regularization method shrinks the text-token and image-patch similarity scores towards zero and improves localization of the relevant clinical findings. We evaluate the resulting model by comparing it to an equivalent unregularized baseline, a fully-supervised baseline, and several state-of-the-art, CLIP-style CXR benchmarks (Tiu et al., 2022; Wang et al., 2022b). We demonstrate that our method results in zero-shot classification improvement across a wide range of clinical findings, setting a new state of the art in many instances.

Generalizable Insights about Machine Learning in the Context of Healthcare

CLIP-style models are a type of self-supervised model which can learn useful image and text representations from paired image and text data without the need for any supervised labels. Our regularization scheme is directly motivated by how radiology reports typically describe findings in CXRs, and thus could be applicable to many related medical imaging problems. In summary, this work makes the following contributions:

- A novel regularization scheme applicable to any model that produces local image and text embeddings. The regularization term shrinks the text-token and image-patch similarity scores towards zero for sparser cross-modality similarities, resulting in improved localization of clinical findings.

- The ability to flexibly modulate this sparsity with two hyperparameters and without requiring external object detection networks unlike many related works. Our approach

can be easily implemented and optimized for other medical imaging problems by tuning these hyperparameters to achieve the level of sparsity desired in the new setting.

- State of the art (SOTA) average zero-shot classification performances on the CheXpert and Padchest datasets, surpassing recently introduced self-supervised models and comparable fully supervised ones, demonstrating the efficacy of our approach in a particular chest x-ray (CXR) setting.

2. Related Work

Many groups have made efforts to produce fine-grained alignment of images and text in CLIP-style models (Yao et al., 2021; Li et al., 2022a; Zhong et al., 2022; Wang et al., 2022a; Huang et al., 2021; Li et al., 2022b). Several of these approaches require a separate region proposal/object detection network (Zhong et al., 2022; Li et al., 2022b,a) and as a result are not directly comparable to our work. Additionally, while often effective for natural images, these objection detection models have not been applied as successfully in medical domains like CXRs.

Other approaches (Wang et al., 2022a; Huang et al., 2021) aim to modify the contrastive loss to better align local representations, but unlike our approach, do not aim to induce *sparsity*. For example, while Huang et al. (2021) and Wang et al. (2022a) both include a local contrastive loss, their approaches potentially allow tokens to be similar to all of the cross-modal tokens. Furthermore, Huang et al. (2021) was shown to have poor performance when evaluated by Tiu et al. (2022), while Wang et al. (2022a) is not yet publicly available for evaluation.

Unlike the previously described approaches, and like our TIER method, the approach in Yao et al. (2021) does induce sparsity at the token and patch level. However, their approach more aggressively forces sparsity by only considering the maximum similarity text token for each image token and vice versa. Conversely, our approach allows us to flexibly modulate the level of sparsity using two tune-able hyperparameters (which could allow us to mimic the effect of Yao et al. (2021) if set extremely high).

3. Methods

3.1. Data

We utilized MIMIC-CXR-JPG (Johnson et al., 2019) to train our models and MS-CXR (Boecking et al., 2022), CheXpert (Irvin et al., 2019) and Padchest (Bustos et al., 2020) to evaluate them.

The MIMIC-CXR-JPG dataset (Johnson et al., 2019) consists of 377,095 CXR samples from 65,379 different patients. Many patients have multiple radiological studies within the dataset, with a single study often containing both a frontal and lateral CXR view. These CXRs were evaluated by radiologists, who wrote detailed reports on the clinical findings they observed as well as a sentence or two describing their overall impression of the imaging. We extracted these *impression* sections from the radiology reports to use as the paired text for our image input. We dropped any samples that were missing this impression section,

leaving us with a total of 319,446 CXR-impression pairs. We split these MIMIC-CXR image-text pairs into training and validation subsets (with approximately 90% training data) and ensured that no patient was represented in both subsets. We additionally leverage the MS-CXR (Boecking et al., 2022) dataset for evaluation, which contains 1153 annotated bounding boxes of various CXR findings for a subset of the MIMIC-CXR images.

For evaluation, we utilized the separate CheXpert (Irvin et al., 2019) dataset with predefined validation and test splits which consisted of 234 and 668 CXRs respectively. These subsets of CheXpert have 14 different clinical labels, determined by consensus of 3 and 5 radiologists respectively. We benchmarked our models' thresholded predictions using labels from an additional 3 radiologists available in the CheXpert test set. For the purposes of our evaluation, we only considered the following 5 clinical labels: Cardiomegaly, Edema, Consolidation, Atelectasis, and Pleural Effusion. These labels were the five competition tasks from the CheXpert competition and the most commonly attempted tasks in the literature, making them a natural set for comparison. We also extracted these labels from the MIMIC-CXR dataset, but we only used them when training our fully supervised CNN baseline; our contrastive models did not have any access to these labels.

We additionally evaluated our models with the Padchest dataset (Bustos et al., 2020), of which we only considered the subset of 39,053 CXRs that were labeled by radiologists. There were over a hundred different labels present in these CXRs, but we focused on the set of 57 labels that were present with frequency of at least 50 in our selected subset, as was done by Tiu et al. (2022).

All images were resized to 224×224 pixels with 3 RGB channels. At train time, we performed random data augmentations including random resizing, cropping, affine transformation, and color jitter, while at test time, we simply resized images to 256×256 before center cropping to 224×224.

3.2. Model Architecture

We based our model on the BioViL architecture (Boecking et al., 2022), which consists of a pre-trained ResNet-50 architecture as the vision encoder and "CXR-BERT-specialized", a transformer, as the text encoder. This model differed from the original CLIP architecture in that it consisted of a radiology-specific text encoder (CXR-BERT) and was trained with an additional MLM loss, among several other changes (Boecking et al., 2022). This model was also trained using MIMIC-CXR and importantly did not have access to the CheXpert or Padchest datasets, which we used for evaluation.

For our purposes, the most critical feature of the BioViL model is that the final ResNet-50 block provides embeddings that correspond to local, connected regions of the input image (see the green path on the top of Figure Fig. 1). Thus, in addition to the single global image embedding, for an input image of size 224×224 this model also produces a set of 49 embeddings in a 7×7 grid, which all share the same joint feature space as the global image embedding. The number of embeddings is a function of the original input size (a larger image input would yield more embeddings) as well as the choice to use the final ResNet block output (using an earlier output would lead to more fine-grained local embeddings). A single multi-layer perceptron with one hidden layer was used to project
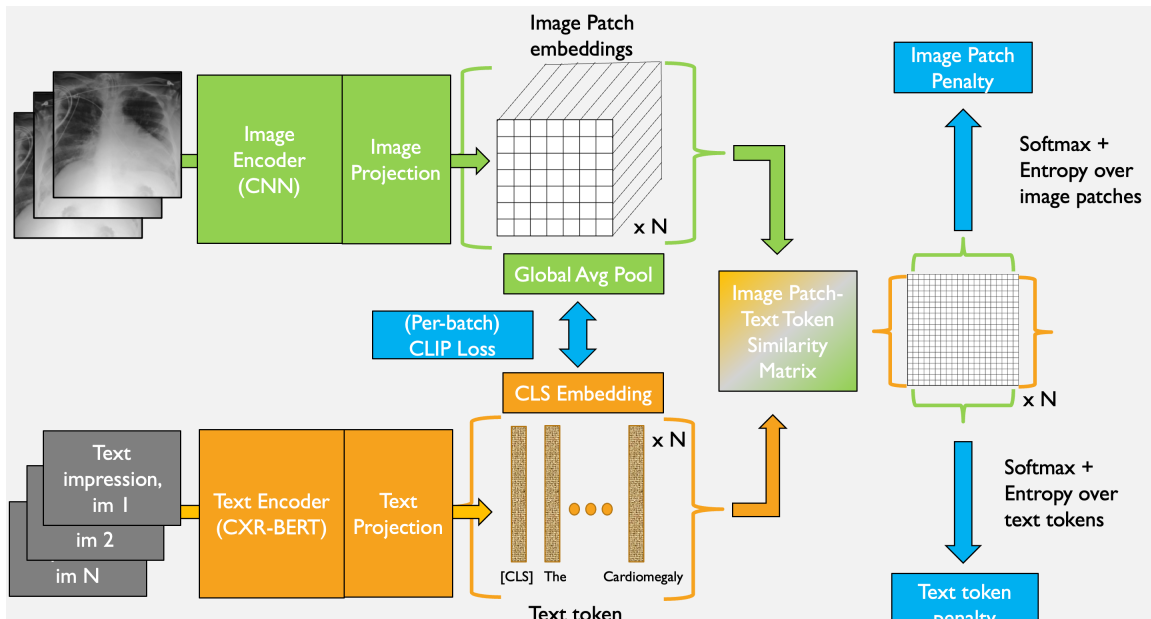
Figure 1: An overview of TIER, our regularized training method. In addition to the standard CLIP loss for the batch, each image-text pair produces a token-wise similarity matrix from which the image patch and text token penalties are computed via softmax + entropy.

each local embedding to the joint feature space. We call these local image embeddings the *patch* embeddings as they correspond to regional patches of the image.

The text transformer naturally produces a text token embedding for each input token to the model. We use a single multi-layer perceptron with one hidden layer to project these text token embeddings to the joint feature space. The projected embedding from the first text token, [CLS], is contrasted with the global image embedding as is done with typical contrastive language-image pre-trained models (Radford et al., 2021; Palepu and Beam, 2022; Zhang et al., 2020). For a training batch of image-text pairs (x^I, x_T), we use the standard CLIP loss as described in Radford et al. (2021). We add additional penalty terms, described in the following section, to regularize our model beyond this standard CLIP loss. The pseudocode for our method is described in Appendix A.

3.3. TIER: Text-Image Entropy Regularization of Image-Patch and Text-Token Similarity Scores

TIER works by first computing a matrix of image-patch and text-token similarities. Specifically, consider an example image-text pair that has $I = \{I_1, \ldots, I_P\}$ image-patch embeddings (in our case, $P = 49$), and has $T = \{T_1, \ldots, T_T\}$ text-token embeddings (T can vary for each sample as captions can be different lengths). We compute the image patch-text token similarity matrix S by computing a $T \times P$ matrix of cosine similarities between each image-patch embedding and text-token embedding. The embeddings for each input modality are the outputs of an encoder model that is specific to that input, e.g. a CNN or vision transformer for images and a BERT-style transformer for text. Importantly, we

select encoders that provide embeddings at the token level, i.e., image-patch embeddings and text-token embeddings. Row i of S indicates the cosine similarity between a text-token T_i and each image patch in I. The columns of S likewise indicate the cosine similarity between a given image patch I_j and each text token in T.

Recall, the goal of our approach is to shrink the elements of S such that each text token is similar to a relatively small number of image patches. To do this, we introduced an entropy-based penalty term that induces shrinkage on the elements of S. First, we perform a row-wise softmax of S and measure the entropy between a text token T_i and all of the image patches in I, shown below:

$$\mathcal{H}(T_i, I) = \sum_{j=1}^{|P|} -p_j * \log(p_j) \tag{1}$$

where p_j is the probability produced by the softmax of the row of S corresponding to T_i. This term will be maximized when each p_j is $\frac{1}{P}$, implying that all of the image patch embeddings have equal similarity to T_i.

Next, we apply the same procedure to the columns of S, applying a column-wise softmax over the text-token similarities to produce probabilities p_1 to p_T for each image patch I_i and calculating the entropy of these probabilities as follows:

$$\mathcal{H}(T, I_j) = \sum_{i=1}^{|T|} -p_i * \log(p_i) \tag{2}$$

We average the $N \times T$ image-patch entropies $\mathcal{H}(T_i, I)$ and the $N \times P$ text-token entropies $\mathcal{H}(T, I_j)$ to produce an *image-patch penalty* and *text-token penalty* for the batch. We control the effects of these penalties on training by weighting them with hyperparameters λ_t and λ_p respectively, adding the weighted penalties to the CLIP loss to compute the total loss.

A grid search over the range $[0, 0.25]$ was used to set the hyperparameters ($\lambda_p = 0.2$, $\lambda_t = 0.1$) for our regularized model. Specifically, we trained our contrastive models for just a single epoch on MIMIC-CXR with pairs of λ_p and λ_t, and chose the pair that maximized zero-shot AUC on the validation set. These results are available in Appendix D. Both the training procedure and zero-shot classification method are described in later sections.

3.4. Training Details

We begin with the pretrained BioViL architecture and model weights, "CXR-BERT-specialized" (Boecking et al., 2022), which has already been trained with contrastive learning on the MIMIC-CXR dataset. In this original training, only frontal images were used, and they used a masked language model (MLM) loss in addition to the CLIP loss. Starting with this pretrained model, we train two separate CLIP-style models: A regularized model in which $\lambda_p = 0.2$ and $\lambda_t = 0.1$, as well as an unregularized baseline model, in which $\lambda_p = \lambda_t = 0$. Despite only minor changes (further training on MIMIC-CXR, inclusion of lateral CXRs, omission of the MLM loss, freezing of early text encoder layers), our unregularized baseline significantly outperformed the publicly available pretrained model from Boecking et al. (2022) as seen in Appendix E.

All aspects of model training are identical between our regularized and unregularized models, other than the additional penalty terms. For both models, we freeze the first 8 layers of the BERT encoder, while leaving the rest of the text encoder and vision encoder unfrozen. Each model is trained for 30 epochs using the loss described in the previous section with a learning rate of 0.0001 and batch size of 32.

We also train a fully supervised CNN baseline, which utilizes the same vision encoder as the contrastive models but has a multilayer perceptron with one hidden layer and five outputs. This supervised baseline still uses MIMIC-CXR for training, but instead of text, it is trained with labels using binary-cross entropy loss with a learning rate of 0.0001 and batch size of 32.

3.5. Zero-shot classification

We employ a zero-shot classification procedure that leverages our text and image encoders to identify labels of interest in the images. Our method begins with the user selecting K_p positive and K_n negative queries for the label of interest, Q. Positive queries $\{Q_{p1}, ..., Q_{pK_p}\}$ are text descriptions indicative of the presence of that label, while negative queries $\{Q_{n1}, ..., Q_{nK_n}\}$ are text descriptions indicative of the absence of that label; examples which we used for the five CheXpert labels are detailed in Appendix G. We pass each positive query through the text encoder, project their [CLS] token embeddings to the joint embedding space, and then average these projected embeddings and re-normalize to a unit norm. We do the same for the negative queries so that we have a single positive $\overline{Q_p}$ and negative $\overline{Q_n}$ query embedding associated with each label that we wish to classify:

$$\overline{Q_p} = \frac{\sum_{j=1}^{K_p} Q_{pj}/K_p}{||\sum_{j=1}^{K_p} Q_{pj}/K_p||} \qquad\qquad \overline{Q_n} = \frac{\sum_{j=1}^{K_n} Q_{nj}/K_n}{||\sum_{i=1}^{K_n} Q_{nj}/K_n||} \qquad (3)$$

For any input image we wish to classify, we use the image encoder to compute its projected global image embedding E_{img} (normalized to unit norm) and take the dot product of this global image embedding with both the positive and negative query embeddings $\overline{Q_p}$ and $\overline{Q_n}$ for every label we wish to predict. We subtract these positive and negative cosine similarity scores to get a zero-shot classification score, Z_Q, for our label of interest.

$$Z_Q = (E_{img} \cdot \overline{Q_p}) - (E_{img} \cdot \overline{Q_n}) \qquad (4)$$

Our zero-shot classification output cannot be interpreted as a probability as its range is between $[-2, 2]$. This is sufficient for assessing discriminative performance of our zero-shot classifiers; however, if one desired a probability output, they could instead apply a softmax to the positive and negative similarity scores as was done by Tiu et al. (2022).

4. Results

4.1. Sparsity of clinical findings

To validate our hypothesis that clinical findings are "sparse" and cover a relatively small portion of the CXRs, we use the MS-CXR dataset and compute the average proportion of each image that is covered by the ground-truth bounding boxes. As seen in Tab. 1, all

Table 1: Using the MS-CXR dataset, which contained annotated bounding boxes of several clinical findings, we compute the proportion of the total image that is covered by these bounding boxes. These results support our sparsity hypothesis for CXR images: we demonstrate that each of these findings typically covers only a small fraction of the CXR. In particular, these are all on average under 20% of the image, with most covering closer to 5% of the image.

Finding	Count	Mean Image Coverage (%)	Standard Deviation (%)
Cardiomegaly	333	17.2	4.2
Edema	87	11.0	8.8
Pleural Effusion	142	5.4	3.3
Consolidation	185	7.1	5.7
Atelectasis	98	6.1	4.2
Lung Opacity	108	5.8	5.3
Pneumonia	231	7.2	3.3
Pneumothorax	264	4.7	4.5

clinical findings in this dataset cover a relatively small portion of the image, with the highest (cardiomegaly) covering about 17% of the image, and the majority covering closer to 5% of the image. Thus, it is reasonable to assume that encouraging sparsity of cross-modal similarities could benefit CLIP-style models.

4.2. Heatmap visualizations of the effect of regularization

Qualitatively, our regularization method is able to achieve the desired shrinkage between image patches and text tokens. Fig. 2, Fig. 3, and Fig. 4 show patch-level zero-shot classification scores (i.e., the score between each image patch and the global [CLS] text token) overlaid on top of two CXRs, one with cardiomegaly and one with pleural effusion. In these heatmaps, red is indicative of a higher zero-shot score, blue is a lower score, gray is a more neutral score, and bounding boxes for the given clinical findings are outlined in yellow.

Important differences between the regularized and unregularized models are apparent when we examine the distribution of blue and red regions of the heatmaps in Fig. 2, Fig. 3, and Fig. 4. For the cardiomegaly-positive image (Fig. 2), the regularized model has high scores primarily on the lower left side of the patient's chest (which corresponds to lower right side of the image), where their heart is located. This lines up well with the bounding box annotations. On the other hand, while the unregularized model also displays high scores in the clinically relevant regions, it has many negative scores outside of this region, indicating that the model's classification is heavily sensitive to these extraneous regions that should be less relevant to the cardiomegaly finding. While we might expect negative scores for a few patches (in particular, regions where the clinical finding could reasonably present itself but is not seen for the given image), we would still expect a majority of the patches outside of the bounding boxes to appear gray (close to 0).

We see similar results on other examples from MS-CXR, including for pleural effusion (Fig. 3), consolidation (Fig. 4), edema (Fig. 9 in Appendix B), and atelectasis (Fig. 10 in
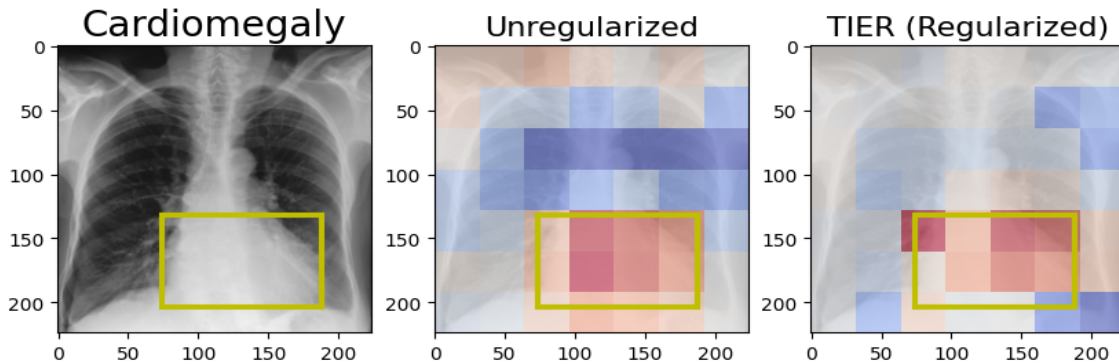
Figure 2: **The penalty term induces shrinkage and improves localization of the image patch-text token similarity scores**. A CXR positive for cardiomegaly, overlaid with heatmaps displaying zero-shot cardiomegaly score for the unregularized (center) and regularized (right) models. Gray corresponds to a neutral (close to zero) zero-shot score, while red is a higher score and blue is a lower score. Compared to the unregularized baseline, the regularized model focuses more on the relevant regions (shown with the bounding box) and less on the irrelevant regions.
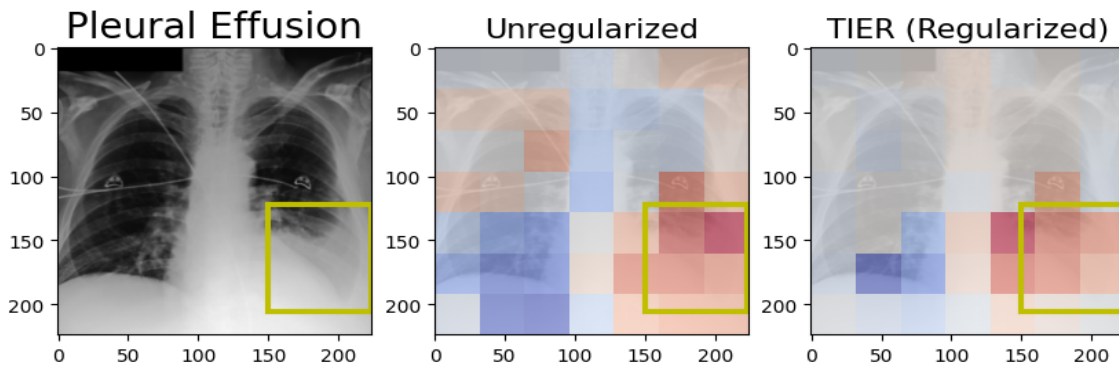

Figure 3: Zero-shot pleural effusion scores for a pleural effusion positive CXR (unreg.: center, TIER: right) with a ground truth bounding box from MS-CXR.
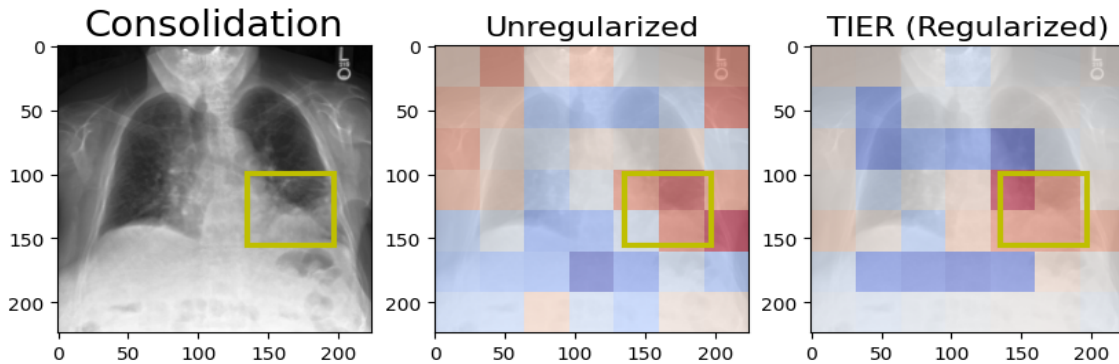

Figure 4: Zero-shot consolidation scores for a consolidation positive CXR (unreg.: center, TIER: right) with a ground truth bounding box from MS-CXR

Appendix B). Across these five clinical findings, the heatmaps with overlaid bounding boxes from MS-CXR suggest that regularization not only induced sparsity, but also improved the localization of clinical findings. For the regularized model, the high (red) scores appear more concentrated within the bounding boxes and scores outside the boxes are relatively less extreme when compared to the unregularized model. We also provide heatmap examples from a separate dataset, CheXpert (Irvin et al., 2019) in Appendix C. Although ground truth bounding boxes are not available for these examples from CheXpert, the image patch-text token similarity scores still appear more sparse and focused on clinically justifiable regions when using the regularized model.

4.3. Distributions of image-patch similarity scores to the global `[CLS]` text token

We further quantify the effect of our regularization method on the image-patch similarities by aggregating results across the entire MS-CXR dataset. In Fig. 5, for each of the chosen five chosen clinical labels, we compare the average image-patch similarity score to the relevant label embedding for patches within the ground truth bounding box to patches outside the bounding box. If a model is focused on the clinically relevant regions, then the similarities inside and outside the box should be more distinct. On the other hand, if a model is not focused on the correct clinically relevant regions, the scores outside the bounding box would overlap with the scores inside the bounding box. As seen in Fig. 5, across all five clinical findings the patch similarity scores are in fact more distinct when using the regularized model than when using the unregularized model. Thus, this analysis suggests that regularization improves the localization of clinical findings.

We further analyze the patch-level similarity scores from our model by utilizing a set of 160 positive image-text pairs from MIMIC-CXR. In Fig. 6, we plot the rank-ordered similarities of the projected [CLS] token embeddings from the radiology report text embedding to the 49 image-patch embeddings of the corresponding images, showing that the regularized model on average has significantly lower similarities to the patch embeddings than the unregularized model. We produce a normalized version of this figure in Fig. 7 by dividing the similarity by the sum of all patch similarities in the entire image. Here, we can see that the regularized model tends to have a few patches with relatively higher similarities to the [CLS] token embedding, and many with relatively lower similarities; this further supports our claim that our regularization scheme shrinks token-level similarities towards zero in order to achieve a lower entropy.

4.4. Zero-shot classification

Next, we evaluated the zero-shot classification performance of both the regularized and unregularized models on the held-out CheXpert test set. Our primary benchmark for these models is the 'CheXzero' model (Tiu et al., 2022), which recently achieved SOTA zero-shot AUC on this task. We use their weights from the checkpoint that achieved the highest AUC on the CheXpert validation set. We also evaluate another recent self-supervised model, MedCLIP (Wang et al., 2022b), with the caveat that this model is not strictly zero-shot because the authors utilized clinical labels during their training process. Additionally, we evaluate a fully supervised CNN that uses our vision encoder with an additional classification
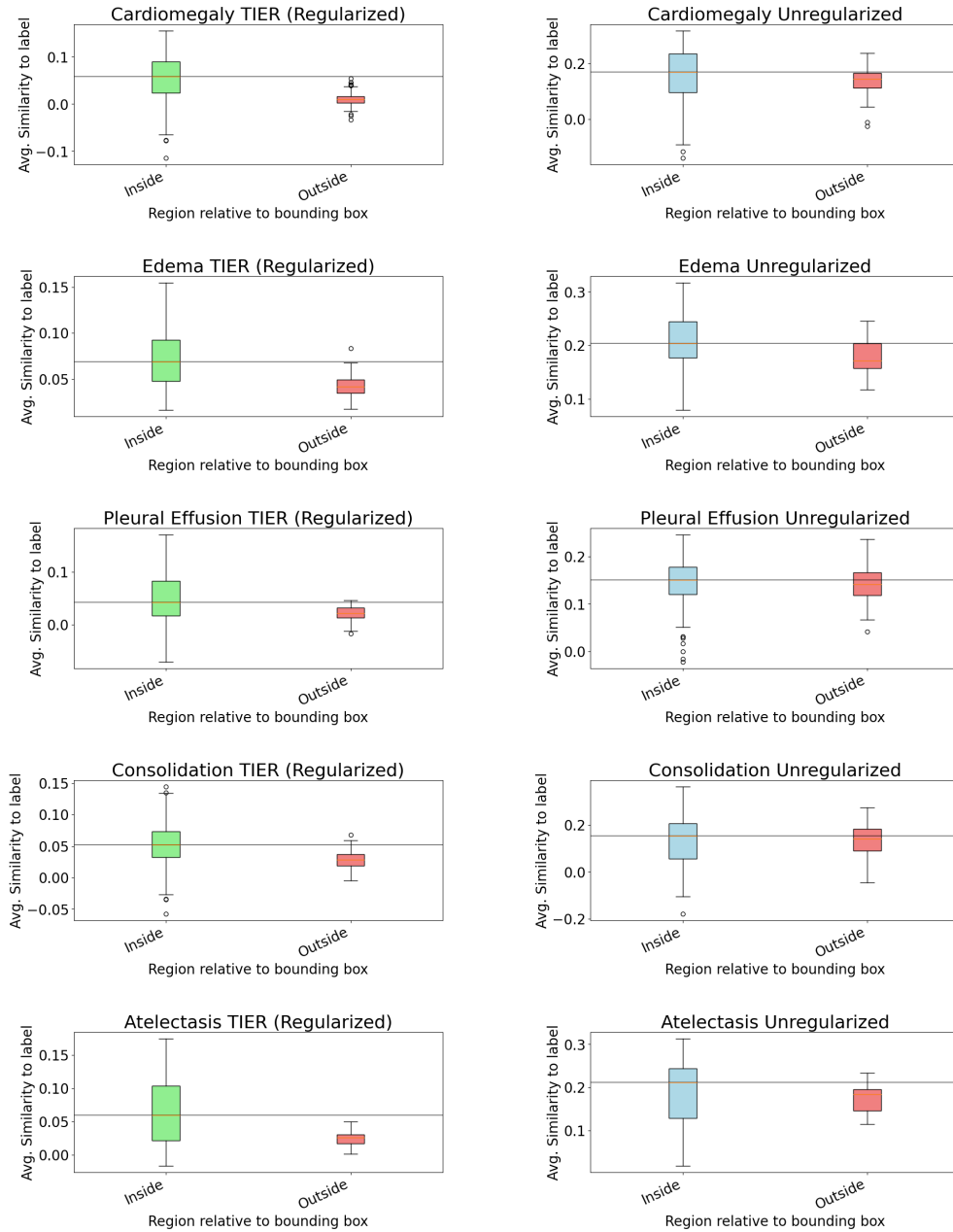
Figure 5: Using the MS-CXR dataset with annotated bounding boxes of findings, we compare the average similarity score for patches inside the bounding boxes to patches outside the bounding boxes. A reference horizontal line is drawn at the level of the median similarity score inside the bounding box. A model that localizes better should have more separation between the similarity scores inside and outside the boxes. For all five labels, these similarities appear significantly more distinct when using the regularized (TIER) model.

Figure 6: The similarities of each patch to the CLS embedding for a set of 160 MIMIC-CXR images, sorted in descending order.
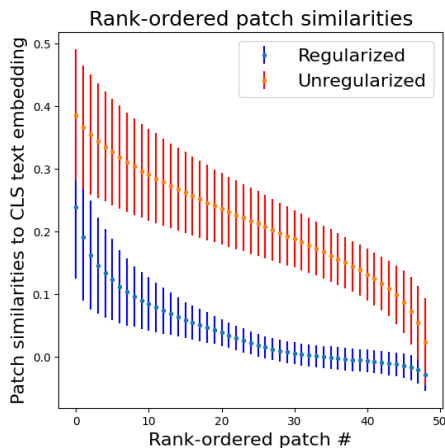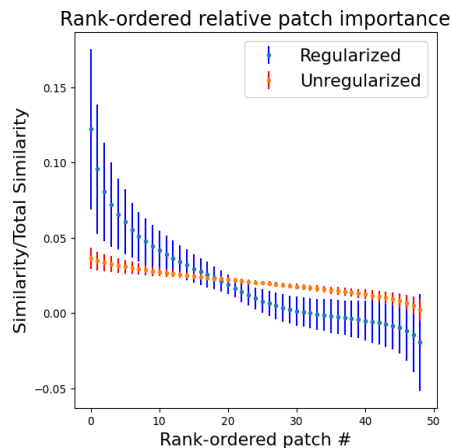
Figure 7: The same plot as Fig. 6 in which each patch-similarity is divided by the sum of the total patch-similarity scores across all patches of an image.

Table 2: Average AUCs for various models on 1000 bootstraps of the CheXpert Test evaluation. The highest zero-shot AUC is bolded (the three on the left are performing zero-shot classification, in which they have never previously seen any labels in the training set). As seen in Appendix F (Tab. 6, Tab. 7, and Tab. 8), all differences between zero-shot models are statistically significant except for Unregularized vs CheXzero for Consolidation. Though MedCLIP is trained with contrastive learning, it also utilizes labels during training so we do not consider it to be fully zero-shot.

Label	TIER(Ours)	Unregularized(Ours)	CheXzero	MedCLIP	Fully Supervised CNN
Average	**0.9033**	0.8972	0.8935	0.8771	0.8888
Cardiomegaly	**0.9171**	0.8924	0.8834	0.8391	0.8640
Edema	**0.9242**	0.9073	0.8942	0.9124	0.9224
Consolidation	0.8971	0.9121	**0.9132**	0.8865	0.8600
Atelectasis	**0.8653**	0.8574	0.8430	0.7942	0.8587
Pleural Effusion	0.9129	0.9168	**0.9337**	0.9531	0.9388

head. We bootstrap 1000 times, randomly sampling the test set with replacement and evaluating the mean AUC performance of each model over these 1000 bootstraps. These results can be seen in Tab. 2, which demonstrates that our regularized model achieves SOTA zero-shot AUC; regularization offers a modest bump in average AUC performance. Excluding "Unregularized vs CheXzero for Consolidation", all pairwise AUC differences between the zero-shot models are statistically significant according to a two sample t-test for the difference of means. These zero-shot models are also competitive against three reference radiologists according to their Matthews's correlation coefficient (MCC) and F1 scores, as seen in Appendix H.

We use the Padchest dataset to evaluate a broader set of findings, specifically looking at the 57 findings with $n \geq 50$ from the radiologist-labeled subset of Padchest. We constructed positive label queries using the phrase "X is present.", while we constructed negative label queries with the phrase "No X.", replacing X with the label of interest. The notable exception was when we classified "normal" images; in this instance, we used "Abnormal findings." as the negative query. Tab. 3 details the Padchest results for the regularized, unregularized, and CheXzero models. As seen in Appendix I(Tab. 10, Tab. 11), our regularized TIER model achieves statistically significant boosts in performance on average as well as for the majority of Padchest findings when compared head-to-head with CheXzero and our unregularized baseline model.

4.5. Zero-shot COVID-19 diagnosis

We also evaluate our model for COVID-19 detection, which is a diagnosis not present in any of our training data. As a result, our models cannot rely on the actual label itself (i.e., the word cardiomegaly in the caption of a cardiomegaly-positive image), and therefore the diagnostic capability of our models on this task can be attributed to their ability to recognize the descriptive attributes being queried. Furthermore, discriminating COVID-19 and non-COVID-19 pneumonia from chest imaging is a difficult and non-trivial task, with one study reporting just a 74% average accuracy for three radiologists using chest CT for this task (Bai et al., 2020).

We created queries to discriminate COVID-19 and non-COVID-19 pneumonia based on differences mentioned in the literature (Bai et al., 2020; Borghesi and Maroldi, 2020). For the positive COVID-19 query, we used the query "Ground glass opacities and consolidation with peripheral distribution with fine reticular opacity and vascular thickening.", and for the negative COVID-19 query, we used "Pleural effusion present with lymphadenopathy and consolidation with central distribution." (which were described by Bai et al. (2020) as findings more specific to non-COVID-19 pneumonia). We achieved zero-shot AUCs of 0.759, 0.753, and 0.752 with the regularized, unregularized, and CheXzero models respectively on discriminating COVID-19 from non-COVID pneumonia within the COVID-QU-Ex Dataset (Tahir et al., 2021, 2022).

This performance indicates that we can leverage our model for difficult classification tasks by simply providing English descriptions of the class-discriminating features. Furthermore, this procedure can easily extend to other labels, meaning self-supervised vision-language architectures such as these could be leveraged to diagnose novel diseases as long as their presentation on imaging can be described in natural language.

5. Discussion

In this work, we introduce a simple and flexible regularization method for contrastive language-image pre-trained models which encourages shrinkage of the image-patch and text-token similarities. We demonstrate how our regularization method improves the localization of clinical findings and can benefit zero-shot performance of these models, training a model that achieves SOTA zero-shot classification performance on a broad set of CXR findings. These improvements are robust across a wide range of tasks relative to many strong benchmarks, though in some instances the improvements are modest. Though our work

Table 3: **Over 1000 bootstraps, the regularized model outperforms the unregularized and CheXzero models in fine-grained finding prediction.** Zero-shot AUCs for 57 padchest findings. The best AUC for each finding across the three tested models is shown in **bold**. As shown in Appendix I(Tab. 10 and Tab. 11), all winners are statistically significant except for CheXzero for the rib fracture finding.

Label	Count	TIER(Ours)	Unregularized(Ours)	CheXzero
Average AUC	39053	**0.7554**	0.7425	0.7263
Number of Evaluations Won (%)	57	**20 (35.1%)**	18 (31.6%)	18 (31.6%)
endotracheal tube	284	0.9796	0.9566	**0.9829**
pleural effusion	1748	0.9420	0.9303	**0.9505**
pulmonary edema	87	0.9413	0.9454	**0.9565**
heart insufficiency	546	0.9261	**0.9272**	0.9178
pulmonary fibrosis	166	**0.9517**	0.9441	0.9218
cardiomegaly	3746	0.8837	0.8833	**0.8905**
vascular redistribution	129	**0.8772**	0.8720	0.7506
consolidation	364	**0.8783**	0.8499	0.8652
hilar congestion	601	**0.8554**	0.8502	0.8257
pulmonary mass	247	0.8441	**0.8723**	0.8421
cavitation	122	**0.8576**	0.7943	0.8534
alveolar pattern	1353	**0.8763**	0.8170	0.7638
calcified pleural thickening	102	**0.8597**	0.8429	0.8507
lung metastasis	89	**0.8774**	0.8608	0.8277
emphysema	376	0.7178	0.7184	**0.8306**
interstitial pattern	1907	0.8351	**0.8404**	0.8164
costophrenic angle blunting	1683	0.7699	**0.8081**	0.6903
COPD signs	4823	0.6509	0.6529	**0.7512**
tuberculosis	59	0.8390	**0.8437**	0.7978
atelectasis	676	0.7817	0.7915	**0.8092**
reticular interstitial pattern	72	0.8445	**0.8676**	0.8224
pneumonia	1780	**0.8138**	0.7966	0.7739
lobar atelectasis	168	0.8084	**0.8157**	0.7751
normal	12694	0.7763	**0.7906**	0.7531
pleural thickening	213	**0.7844**	0.7546	0.7525
reticulonodular interstitial pattern	51	**0.8623**	0.8384	0.8414
infiltrates	1456	0.7429	0.7354	**0.7478**
hypoexpansion	166	0.8534	**0.8715**	0.7946
hypoexpansion basal	119	**0.8897**	0.8745	0.8018
humeral fracture	81	0.7423	0.6729	**0.7491**
pneumothorax	98	0.7306	0.7285	**0.7774**
multiple nodules	102	0.7908	**0.8529**	0.7169
hyperinflated lung	197	0.7009	0.6677	**0.7132**
bronchiectasis	667	0.7346	**0.7440**	0.6901
adenopathy	136	0.6787	**0.7311**	0.7039
mediastinal enlargement	106	0.7254	0.6668	**0.7593**
laminar atelectasis	1378	0.6734	**0.6878**	0.6793
vertebral compression	126	0.7240	**0.7344**	0.6464
rib fracture	140	0.6898	0.6681	0.6910
tuberculosis sequelae	185	**0.7969**	0.7738	0.5843
hilar enlargement	447	**0.7218**	0.7147	0.6786
tracheal shift	180	0.6158	0.5007	**0.6344**
mediastinal mass	74	**0.7098**	0.4095	0.6477
central vascular redistribution	63	**0.7289**	0.5674	0.3545
vertebral fracture	104	0.7914	**0.8601**	0.4997
superior mediastinal enlargement	153	0.5510	**0.6379**	0.5969
vascular hilar enlargement	1428	**0.6256**	0.6042	0.6239
nodule	736	0.4463	0.5079	**0.5467**
air trapping	1952	0.5804	**0.6315**	0.5809
bullas	192	**0.7446**	0.5848	0.4865
ground glass pattern	123	**0.6713**	0.6612	0.6028
calcified adenopathy	124	**0.6738**	0.6242	0.5836
minor fissure thickening	127	0.6004	0.5583	**0.7732**
unchanged	4036	0.6182	**0.6339**	0.3955
clavicle fracture	74	0.5970	0.5960	**0.6075**
pseudonodule	795	0.4770	0.4723	**0.5580**
end on vessel	63	0.3976	0.4851	**0.5606**

is confined to the CXR setting, we believe it should be broadly applicable to many other areas where CLIP-style models can be used, such as other medical imaging tasks and even applications outside of medicine. We believe our work contributes to a growing literature (Kumar et al., 2022; Mu et al., 2022; Meier et al., 2021) seeking to augment and improve CLIP-style models with inductive biases and domain-specific observations.

Limitations   While regularization does result in a statistically significant increase in average zero-shot AUC, these improvements are modest and several clinical findings still seem to be better identified with the unregularized baseline or CheXzero models. Nevertheless, the regularized model still represents a state-of-the-art for zero-shot CXR classification and is competitive with its fully-supervised counterpart. Another limitation is that though we demonstrate that regularization induces cross-modal token sparsity and seemingly better localization of the clinical findings, more investigation is needed to confirm whether or not this improved localization would translate to better performance on downstream tasks such as object detection.

References

Harrison X Bai, Ben Hsieh, Zeng Xiong, Kasey Halsey, Ji Whae Choi, Thi My Linh Tran, Ian Pan, Lin-Bo Shi, Dong-Cui Wang, Ji Mei, et al. Performance of radiologists in differentiating covid-19 from non-covid-19 viral pneumonia at chest ct. *Radiology*, 296 (2):E46–E54, 2020.

Benedikt Boecking, Naoto Usuyama, Shruthi Bannur, Daniel C Castro, Anton Schwaighofer, Stephanie Hyland, Maria Wetscherek, Tristan Naumann, Aditya Nori, Javier Alvarez-Valle, et al. Making the most of text semantics to improve biomedical vision–language processing. *arXiv preprint arXiv:2204.09817*, 2022.

Andrea Borghesi and Roberto Maroldi. Covid-19 outbreak in italy: experimental chest x-ray scoring system for quantifying and monitoring disease progression. *La radiologia medica*, 125(5):509–513, 2020.

Aurelia Bustos, Antonio Pertusa, Jose-Maria Salinas, and Maria de la Iglesia-Vayá. Padchest: A large chest x-ray image dataset with multi-label annotated reports. *Medical image analysis*, 66:101797, 2020.

Alexey Dosovitskiy, Lucas Beyer, Alexander Kolesnikov, Dirk Weissenborn, Xiaohua Zhai, Thomas Unterthiner, Mostafa Dehghani, Matthias Minderer, Georg Heigold, Sylvain Gelly, et al. An image is worth 16x16 words: Transformers for image recognition at scale. *arXiv preprint arXiv:2010.11929*, 2020.

Kaiming He, Xiangyu Zhang, Shaoqing Ren, and Jian Sun. Deep residual learning for image recognition. In *Proceedings of the IEEE conference on computer vision and pattern recognition*, pages 770–778, 2016.

Shih-Cheng Huang, Liyue Shen, Matthew P Lungren, and Serena Yeung. Gloria: A multimodal global-local representation learning framework for label-efficient medical image

recognition. In *Proceedings of the IEEE/CVF International Conference on Computer Vision*, pages 3942–3951, 2021.

Jeremy Irvin, Pranav Rajpurkar, Michael Ko, Yifan Yu, Silviana Ciurea-Ilcus, Chris Chute, Henrik Marklund, Behzad Haghgoo, Robyn Ball, Katie Shpanskaya, et al. Chexpert: A large chest radiograph dataset with uncertainty labels and expert comparison. In *Proceedings of the AAAI conference on artificial intelligence*, volume 33, pages 590–597, 2019.

Alistair EW Johnson, Tom J Pollard, Nathaniel R Greenbaum, Matthew P Lungren, Chih-ying Deng, Yifan Peng, Zhiyong Lu, Roger G Mark, Seth J Berkowitz, and Steven Horng. Mimic-cxr-jpg, a large publicly available database of labeled chest radiographs. *arXiv preprint arXiv:1901.07042*, 2019.

Bhawesh Kumar, Anil Palepu, Rudraksh Tuwani, and Andrew Beam. Towards reliable zero shot classification in self-supervised models with conformal prediction. *arXiv preprint arXiv:2210.15805*, 2022.

Juncheng Li, Xin He, Longhui Wei, Long Qian, Linchao Zhu, Lingxi Xie, Yueting Zhuang, Qi Tian, and Siliang Tang. Fine-grained semantically aligned vision-language pre-training. *arXiv preprint arXiv:2208.02515*, 2022a.

Liunian Harold Li, Pengchuan Zhang, Haotian Zhang, Jianwei Yang, Chunyuan Li, Yiwu Zhong, Lijuan Wang, Lu Yuan, Lei Zhang, Jenq-Neng Hwang, et al. Grounded language-image pre-training. In *Proceedings of the IEEE/CVF Conference on Computer Vision and Pattern Recognition*, pages 10965–10975, 2022b.

Joshua Meier, Roshan Rao, Robert Verkuil, Jason Liu, Tom Sercu, and Alex Rives. Language models enable zero-shot prediction of the effects of mutations on protein function. *Advances in Neural Information Processing Systems*, 34:29287–29303, 2021.

Norman Mu, Alexander Kirillov, David Wagner, and Saining Xie. Slip: Self-supervision meets language-image pre-training. In *European Conference on Computer Vision*, pages 529–544. Springer, 2022.

Anil Palepu and Andrew L Beam. Self-supervision on images and text reduces reliance on visual shortcut features. *arXiv preprint arXiv:2206.07155*, 2022.

Alec Radford, Jong Wook Kim, Chris Hallacy, Aditya Ramesh, Gabriel Goh, Sandhini Agarwal, Girish Sastry, Amanda Askell, Pamela Mishkin, Jack Clark, et al. Learning transferable visual models from natural language supervision. In *International Conference on Machine Learning*, pages 8748–8763. PMLR, 2021.

Anas M Tahir, Muhammad EH Chowdhury, Amith Khandakar, Tawsifur Rahman, Yazan Qiblawey, Uzair Khurshid, Serkan Kiranyaz, Nabil Ibtehaz, M Sohel Rahman, Somaya Al-Maadeed, et al. Covid-19 infection localization and severity grading from chest x-ray images. *Computers in biology and medicine*, 139:105002, 2021.

Anas M. Tahir, Muhammad E. H. Chowdhury, Yazan Qiblawey, Amith Khandakar, Tawsi-fur Rahman, Serkan Kiranyaz, Uzair Khurshid, Nabil Ibtehaz, Sakib Mahmud, and Maymouna Ezeddin. Covid-qu-ex dataset, 2022. URL https://www.kaggle.com/dsv/3122958.

Ekin Tiu, Ellie Talius, Pujan Patel, Curtis P Langlotz, Andrew Y Ng, and Pranav Ra-jpurkar. Expert-level detection of pathologies from unannotated chest x-ray images via self-supervised learning. *Nature Biomedical Engineering*, pages 1–8, 2022.

Ashish Vaswani, Noam Shazeer, Niki Parmar, Jakob Uszkoreit, Llion Jones, Aidan N Gomez, Łukasz Kaiser, and Illia Polosukhin. Attention is all you need. *Advances in neural information processing systems*, 30, 2017.

Fuying Wang, Yuyin Zhou, Shujun Wang, Varut Vardhanabhuti, and Lequan Yu. Multi-granularity cross-modal alignment for generalized medical visual representation learning. *arXiv preprint arXiv:2210.06044*, 2022a.

Zifeng Wang, Zhenbang Wu, Dinesh Agarwal, and Jimeng Sun. Medclip: Contrastive learning from unpaired medical images and text. *arXiv preprint arXiv:2210.10163*, 2022b.

Lewei Yao, Runhui Huang, Lu Hou, Guansong Lu, Minzhe Niu, Hang Xu, Xiaodan Liang, Zhenguo Li, Xin Jiang, and Chunjing Xu. Filip: fine-grained interactive language-image pre-training. *arXiv preprint arXiv:2111.07783*, 2021.

Yuhao Zhang, Hang Jiang, Yasuhide Miura, Christopher D Manning, and Curtis P Langlotz. Contrastive learning of medical visual representations from paired images and text. *arXiv preprint arXiv:2010.00747*, 2020.

Yiwu Zhong, Jianwei Yang, Pengchuan Zhang, Chunyuan Li, Noel Codella, Liunian Harold Li, Luowei Zhou, Xiyang Dai, Lu Yuan, Yin Li, et al. Regionclip: Region-based language-image pretraining. In *Proceedings of the IEEE/CVF Conference on Computer Vision and Pattern Recognition*, pages 16793–16803, 2022.

Appendix A. Regularization pseudocode

```python
def regularized_loss(Ims, Txts, lambda_patch, lambda_token):
    # image_encoder - ResNet-50, text_encoder - CXR-BERT-specialized
    # Ims[n, h, w, c], Txts[n, l] - minibatch of aligned images & texts
    # W_i[d_i, d_e] - learned projections of image patches to embed
    # W_t[d_t, d_e] - learned projections of text tokens to embed
    # P - number of image patches, T - number of text tokens

    # Setup; compute patch and token representations
    patch_f = image_encoder(Ims) #[n, d_i, P]
    token_f = text_encoder(Txts) #[n, d_t, T]
    # project to joint embedding space [d_e] and normalize
    patch_e = l2_normalize(dot(patch_f, W_i), axis=1) #[n, d_e, P]
    token_e = l2_normalize(dot(token_f, W_t), axis=1) #[n, d_e, T]

    # CLIP Loss; Compute global embeddings
    image_e = l2_normalize(mean(patch_e, dim=2), axis=1) #[n, d_e]
    text_e = token_e[:, :, 0] #[n, d_e]
    # Compute scaled pairwise cosine similarity matrix
    clip_logits = dot(image_e, text_e.T) * exp(t) #[n, n]
    # Evaluate symmetric CLIP loss function
    labels = np.arange(n)
    loss_i = cross_entropy_loss(clip_logits, labels, axis=0)
    loss_t = cross_entropy_loss(clip_logits, labels, axis=1)
    clip_loss = (loss_i + loss_t)/2

    # Regularization; Compute patch-token similarity matrix
    sim_matrix = batch_multiply(token_e, patch_e) #[n, T, P]
    # Compute patch and token penalties
    patch_entropies = entropy(softmax(sim_matrix, axis = 2)) #[n, T]
    patch_penalty = lambda_patch * mean(patch_entropies)
    token_entropies = entropy(softmax(sim_matrix, axis = 1)) #[n, P]
    token_penalty = lambda_token * mean(token_entropies)

    regularized_loss = clip_loss + patch_penalty + token_penalty
    return regularized_loss
```

Figure 8: Pseudocode for our TIER regularization method. lambda_patch and lambda_token are hyperparameters that can be tuned depending on the desired level of patch/text-token sparsity.

Appendix B. Additional heatmaps demonstrating improved localization in MS-CXR

Across the five clinical findings (Fig. 2, Fig. 3, Fig. 4,Fig. 9, Fig. 10), the heatmaps on bounding-box annotated CXRs suggest that regularization induced sparsity and improved localization of clinical findings. The high (red) scores appear more concentrated within the bounding boxes, and scores outside these boxes are relatively less extreme when compared to the unregularized model.
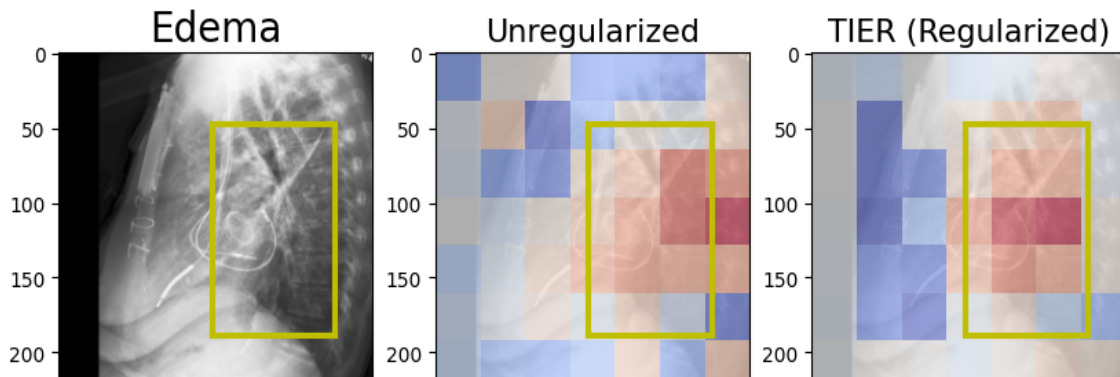

Figure 9: Zero-shot edema scores (blue = negative, red = positive) for an edema positive CXR, (unregularized: center, TIER: right). A yellow bounding box outlines the finding.
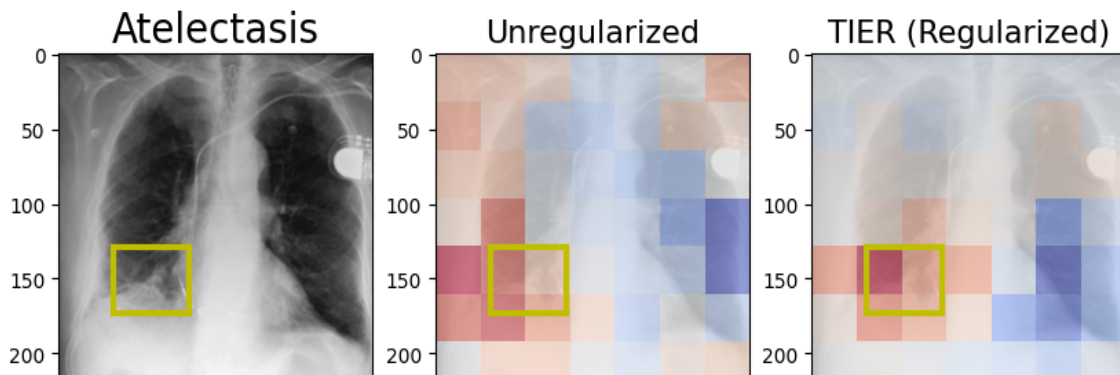

Figure 10: Zero-shot atelectasis scores for an atelectasis positive CXR (unregularized: center, TIER: right). A yellow bounding box outlines the finding.

Appendix C. Additional CheXpert heatmaps

These heatmaps (Fig. 11, Fig. 12, Fig. 13,Fig. 14, Fig. 15) from the CheXpert dataset further suggest that our regularization method induces sparsity of the cross-modal similarity scores. We see fewer red (high score) and blue (low score) patches when we use the regularized model, and far more gray (neutral score) patches.
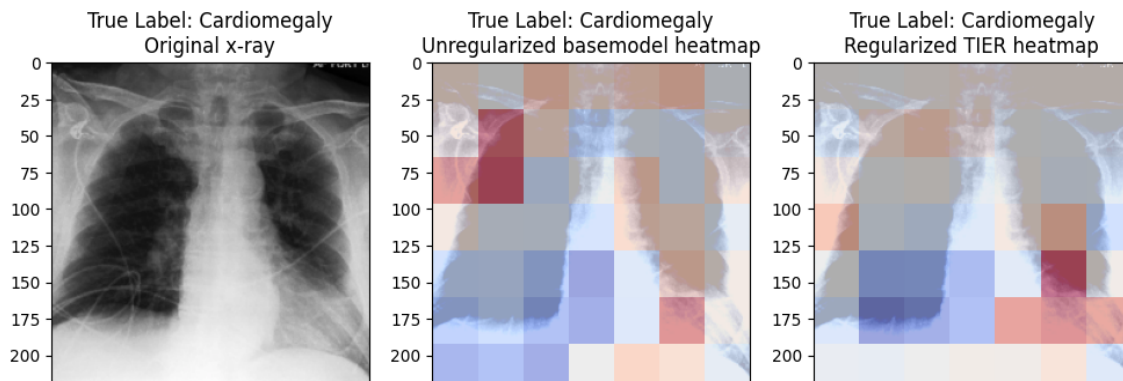

Figure 11: Zero-shot cardiomegaly scores for a cardiomegaly positive CXR, (unregularized: center, TIER: right). Gray is a neutral (close to zero) zero-shot score, while red is higher and blue is lower.
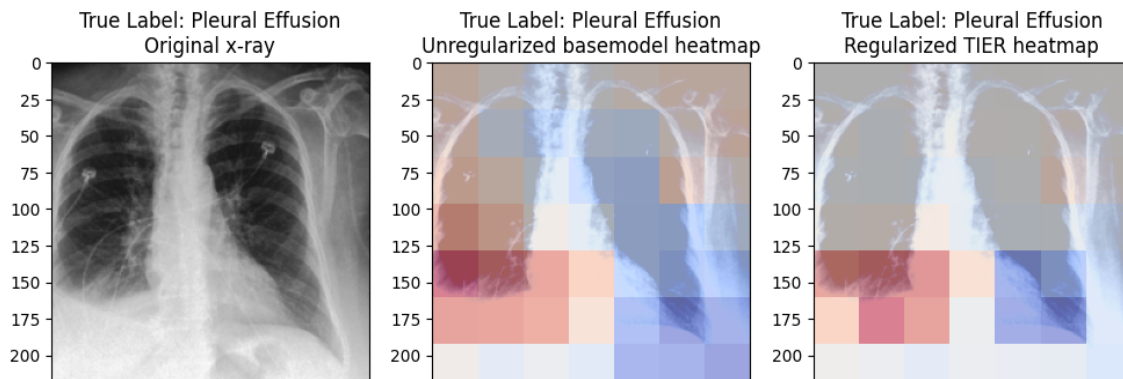
Figure 12: Zero-shot pleural effusion scores for an pleural effusion positive CXR (unregularized: center, TIER: right)
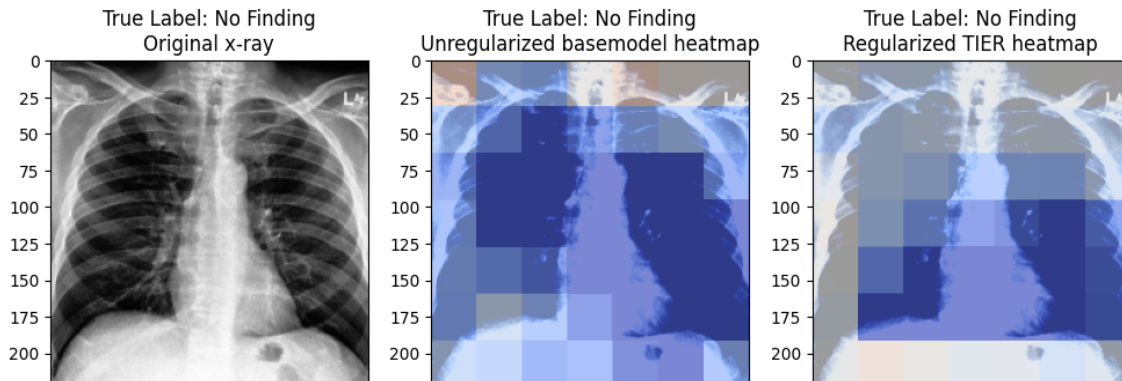
Figure 13: Zero-shot cardiomegaly scores for a cardiomegaly **negative** CXR, (unregularized: center, TIER: right). Gray is a neutral (close to zero) zero-shot score, while red is higher and blue is lower. Because this image is negative for cardiomegaly, we expect low zero-shot scores as is seen. However, it is more desirable for the model to have negative similarities only in the regions where one might normally expect to identify cardiomegaly, and the regularized model better exemplifies this.

Figure 14: Zero-shot atelectasis scores for an atelectasis positive CXR (unregularized: center, TIER: right)

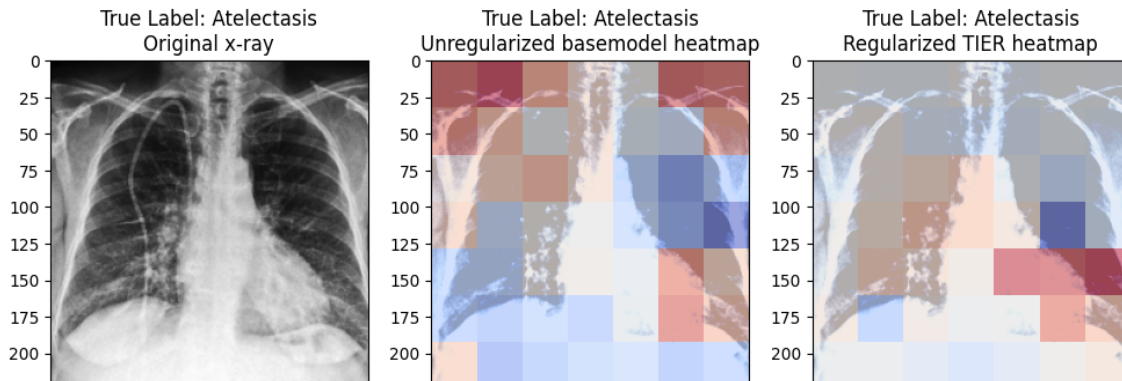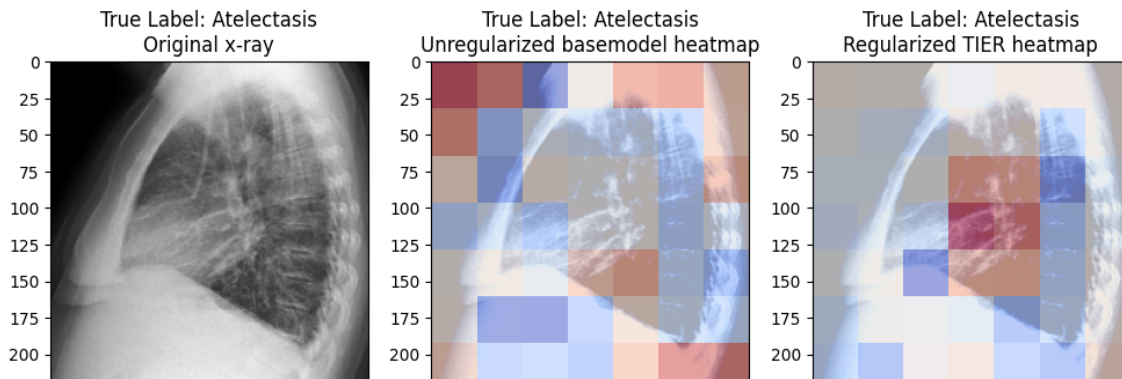Figure 15: A lateral view of the previous atelectasis-positive CXR in Fig. 10, with zero-shot scores overlayed

Appendix D. Regularization Hyperparameter Sweep

Here, we present the results of the hyperparameter sweep we used to select our lambda hyperparameters. Models were trained for a single epoch on MIMIC-CXR, and we use lambda values which maximized zero-shot AUC on the CheXpert validation set to train our regularized TIER model.

Table 4: Zero-shot AUCs on the validation set after training a model with the given hyperparameters for 1 epoch on MIMIC-CXR. ($\lambda_p = 0.20$, $\lambda_t = 0.10$) were chosen to train our regularized TIER model.

λ_p — λ_t	$\lambda_t = 0.00$	$\lambda_t = 0.05$	$\lambda_t = 0.10$	$\lambda_t = 0.15$	$\lambda_t = 0.20$	$\lambda_t = 0.25$
$\lambda_p = 0.00$	0.84708	0.84514	0.84624	0.84272	0.84870	0.83311
$\lambda_p = 0.05$	0.85137	0.84661	0.84353	0.84542	0.84459	0.84712
$\lambda_p = 0.10$	0.83971	0.85457	0.85059	0.84736	0.84464	0.83879
$\lambda_p = 0.15$	0.83774	0.85367	0.85107	0.84174	0.83895	0.84242
$\lambda_p = 0.20$	0.84399	0.85387	**0.85469**	0.84488	0.84747	0.83234
$\lambda_p = 0.25$	0.84901	0.83306	0.84802	0.83939	0.83307	0.85160

Appendix E. Additional chexpert baselines

Here we display some additional baselines on CheXpert test set. In particular, we present the pretrained model we are using (Boecking et al., 2022) and CLIP (Radford et al., 2021).

Table 5: The highest zero-shot AUC is bolded. All models are performing zero-shot classification, meaning they have never explicitly been trained with any labels.

Label	TIER (Ours)	Unregularized (Ours)	BioViL	CLIP
Average	**0.903336**	0.89721	0.63631	0.54056
Cardiomegaly	**0.91714**	0.89239	0.63300	0.56232
Edema	**0.92423**	0.90729	0.58706	0.5028
Consolidation	0.89712	**0.91213**	0.705898	0.6541
Atelectasis	**0.86531**	0.85741	0.58698	0.51719
Pleural Effusion	0.91290	**0.91681**	0.66864	0.46638

Appendix F. P-values for Chexpert evaluation

Here we present the p-values obtained from two-sample t-tests for differences in mean AUCs between TIER (Ours), CheXzero, and the unregularized baseline (Ours) for the chexpert evaluations.

Table 6: Two sample t-test for the difference of means between TIER (Ours) and CheXzero for n = 1000 bootstraps of the chexpert evaluation. All results are significant at the p=0.0001 level.

Label	CheXzero Mean	CheXzero Std	TIER (Ours) Mean	TIER Std	T statistic	P value
Average AUC	0.893494	0.00696	**0.903336**	0.007213	31.05041349	**4.5448E-173**
Cardiomegaly	0.883397	0.013806	**0.917135**	0.010944	60.5584468	**0**
Edema	0.894235	0.015879	**0.924225**	0.01217	47.40345097	**0**
Consolidation	**0.913176**	0.014555	0.897116	0.023315	-18.47763326	**1.67297E-70**
Atelectasis	0.842985	0.015325	**0.865306**	0.014135	33.85648614	**5.547E-199**
Pleural Effusion	**0.933676**	0.010558	0.912898	0.012155	-40.81063492	**2.4219E-265**

Table 7: Two sample t-test for the difference of means between TIER (ours) and the unregularized baseline (ours) for n = 1000 bootstraps of chexpert evaluation. All results are significant at the p=0.0001 level.

Label	Unreg. (Ours) Mean	Unreg. Std	TIER (Ours) Mean	TIER Std	T statistic	P value
Average AUC	0.897206	0.007486	**0.903336**	0.007213	18.64716405	**1.13364E-71**
Cardiomegaly	0.892394	0.012546	**0.917135**	0.010944	46.99391106	**0**
Edema	0.907286	0.013561	**0.924225**	0.01217	29.39763772	**3.6269E-158**
Consolidation	**0.912127**	0.024044	0.897116	0.023315	-14.17328934	**1.60039E-43**
Atelectasis	0.857408	0.014522	**0.865306**	0.014135	12.32428706	**1.08563E-33**
Pleural Effusion	**0.916813**	0.011588	0.912898	0.012155	-7.372034693	**2.44822E-13**

Table 8: Two sample t-test for the difference of means between unregularized (ours) and CheXzero for n = 1000 bootstraps of chexpert evaluation. All results but consolidation are significant at the p=0.0001 level.

Label	CheXzero Mean	CheXzero Std	Unreg. (Ours) Mean	Unreg. Std	T statistic	P value
Average AUC	0.893494	0.00696	**0.897206**	0.007486	11.48385375	**1.32063E-29**
Cardio	0.883397	0.013806	**0.892394**	0.012546	15.25117349	**9.17475E-50**
Edema	0.894235	0.015879	**0.907286**	0.013561	19.7641868	**1.47602E-79**
Consolidation	0.913176	0.014555	0.912127	0.024044	-1.180245623	0.238043032
Atelectasis	0.842985	0.015325	**0.857408**	0.014522	21.60293691	**3.44293E-93**
Pleural Effusion	**0.933676**	0.010558	0.916813	0.011588	-34.01616352	**1.7778E-200**

Appendix G. Chexpert Queries

Table 9: Query captions used for zero-shot classification. No Finding captions are used as the negative queries, while the rest are used as positive queries for their respective labels.

Class Label	Caption
Cardiomegaly	Cardiomegaly is present. The heart shadow is enlarged. The cardiac silhouette is enlarged.
Pleural Effusion	Pleural Effusion is present. Blunting of the costophrenic angles represents pleural effusions. The pleural space is filled with fluid. Layering pleural effusions are present.
Edema	Edema is present. Increased fluid in the alveolar wall indicates pulmonary edema.
Consolidation	Consolidation is present. Dense white area of right lung indicative of consolidation.
Atelectasis	Atelectasis is present. Basilar opacity and volume loss is likely due to atelectasis.
No Finding	The lungs are clear. No abnormalities are present. The chest is normal. No clinically significant radiographic abnormalities. No radiographically visible abnormalities in the chest.

Appendix H. Chexpert Radiologist benchmarking

Comparing zero-shot models against 3 radiologists using MCC and F1 metrics.

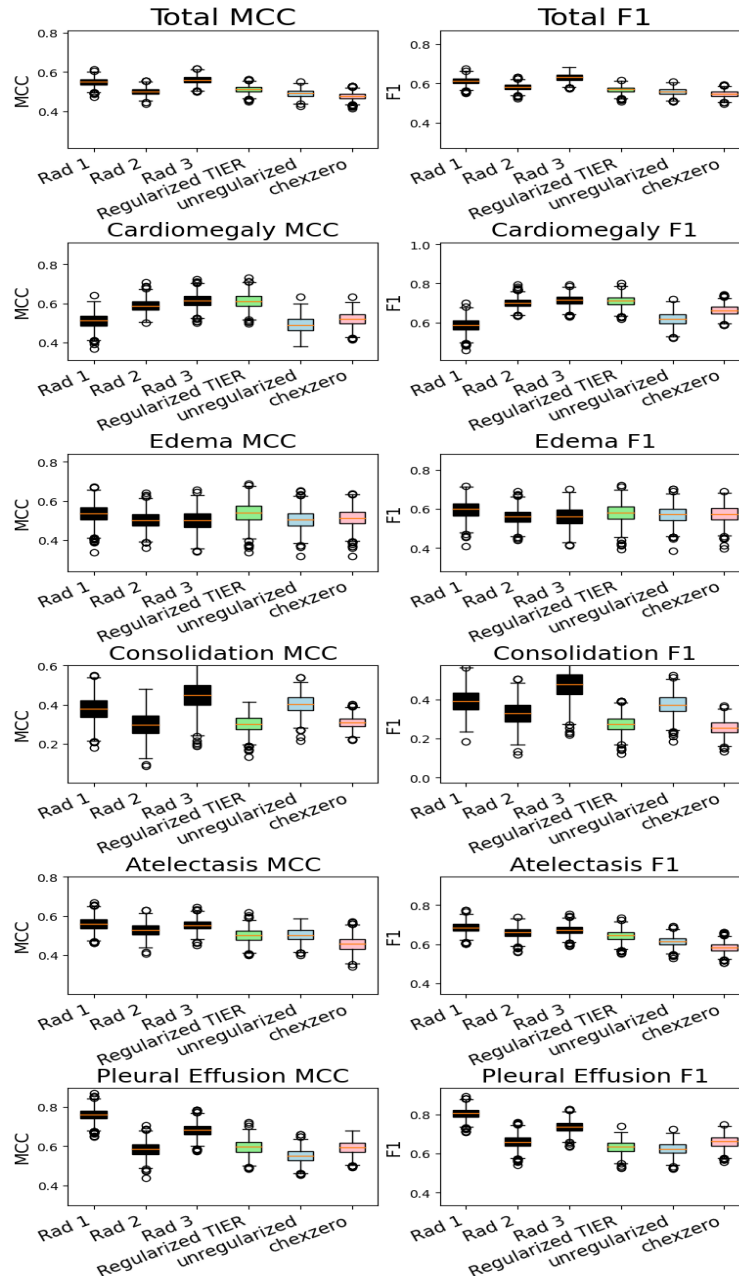Figure 16: Benchmarking thresholded scores against radiologists. MCC (Matthews correlation coefficient) scores and F1 scores for the three zero-shot models (thresholds chosen with val set) and three radiologists are shown. The zero-shot models are competitive with radiologists for most labels. While TIER usually outperforms both the unregularized baseline at CheXzero on both metrics, it is equivalent or worse in several cases.

Appendix I. P-values for padchest evaluation

Here we present the p-values obtained from two-sample t-tests for differences in mean AUCs for n = 1000 bootstraps between the various models for the Padchest evaluations. Comparing CheXzero to TIER (Ours) on Padchest head-to-head:

Table 10: Two sample t-test for the difference of mean AUCs for our padchest evaluation. In this table, we compare the previous SOTA, CheXzero, with our regularized model, TIER. Each model had AUC evaluated on n = 1000 bootstraps of the radiologists-labeled subset of padchest. All but the air trapping, rib fracture, and pulmonary mass results are significant at the p=0.0001 level. TIER wins for 33 findings, achieving an average AUC of 0.755, while CheXzero wins for 21 findings, achieving a lower average AUC of 0.726.

Label	CheXzero Mean	CheXzero Std	TIER (Ours) Mean	TIER Std	T statistic	P value
Average AUC	0.726306	0.002558	**0.75542**	0.002347	265.2017626	**0**
Number won	21		**33**			
endotracheal tube	**0.98295**	0.002315	0.979606	0.005919	-16.63830145	**2.56865E-58**
pleural effusion	**0.950519**	0.002734	0.942045	0.002976	-66.3097905	**0**
pulmonary edema	**0.95646**	0.008905	0.941289	0.008719	-38.49466433	**5.1755E-243**
heart insufficiency	0.917819	0.004761	**0.926097**	0.005453	36.16180694	**1.015E-220**
pulmonary fibrosis	0.921793	0.008352	**0.951654**	0.0054	94.94482215	**0**
cardiomegaly	**0.890467**	0.002511	0.883692	0.002718	-57.89827507	**0**
vascular redistribution	0.750592	0.018104	**0.877236**	0.013662	176.5761336	**0**
consolidation	0.865175	0.009475	**0.878342**	0.009453	31.10977089	**1.3088E-173**
hilar congestion	0.825707	0.007219	**0.855435**	0.008915	81.95062909	**0**
pulmonary mass	0.842056	0.01203	0.844107	0.012986	3.663919249	0.000254856
cavitation	0.853367	0.01575	**0.857639**	0.015601	6.093824451	**1.31926E-09**
alveolar pattern	0.763811	0.006956	**0.87631**	0.005049	413.89493	**0**
calcified pleural thickening	0.850707	0.019816	**0.859651**	0.020362	9.95447536	**8.11361E-23**
lung metastasis	0.827675	0.024452	**0.877375**	0.015578	54.20861509	**0**
emphysema	**0.830578**	0.009475	0.717841	0.013142	-220.0452111	**0**
interstitial pattern	0.816432	0.005126	**0.835144**	0.005382	79.61342323	**0**
costophrenic angle blunting	0.69029	0.006777	**0.769921**	0.006022	277.7581639	**0**
tuberculosis	0.7978	0.027473	**0.838961**	0.020022	38.28895091	**4.8878E-241**
atelectasis	**0.809232**	0.009106	0.781707	0.008707	-69.08700011	**0**
reticular interstitial pattern	0.822429	0.021108	**0.844479**	0.022699	22.49540647	**4.4633E-100**
pneumonia	0.773941	0.005566	**0.813796**	0.004699	173.0195883	**0**
lobar atelectasis	0.775147	0.017958	**0.808411**	0.014991	44.96696255	**1.1767E-305**
normal	0.753171	0.002546	**0.776328**	0.003632	165.0977062	**0**
pleural thickening	0.752537	0.016871	**0.784428**	0.014559	45.25503582	**0**
reticulonodular interstitial pattern	0.841414	0.027064	**0.862346**	0.024737	18.05301834	**1.31327E-67**
infiltrates	**0.747836**	0.006206	0.742854	0.006681	-17.27714913	**1.9175E-62**
hypoexpansion	0.794564	0.014337	**0.853423**	0.011148	102.4871616	**0**
hypoexpansion basal	0.8018	0.015611	**0.889652**	0.013677	133.8542388	**0**
humeral fracture	**0.749084**	0.023222	0.742305	0.026582	-6.07337803	**1.49532E-09**
pneumothorax	**0.777442**	0.018202	0.730643	0.026112	-46.49431338	**0**
multiple nodules	0.716911	0.028257	**0.790815**	0.021245	66.10682237	**0**
hyperinflated lung	**0.713202**	0.018784	0.700879	0.018276	-14.8691189	**1.64612E-47**
bronchiectasis	0.690117	0.01037	**0.734643**	0.009854	98.42837415	**0**
adenopathy	**0.703924**	0.02035	0.678726	0.016664	-30.29508782	**3.2002E-166**
mediastinal enlargement	**0.759299**	0.022403	0.72538	0.026617	-30.83087996	**4.5077E-171**
laminar atelectasis	**0.679276**	0.006312	0.67343	0.006914	-19.74676158	**1.97007E-79**
vertebral compression	0.646448	0.025325	**0.723955**	0.018277	78.47811851	**0**
rib fracture	0.691037	0.020514	0.689835	0.022485	-1.248835772	0.211871446
tuberculosis sequelae	0.584302	0.019415	**0.796895**	0.013529	284.0954171	**0**
hilar enlargement	0.678564	0.012333	**0.721779**	0.011469	81.14282586	**0**
tracheal shift	**0.634359**	0.019985	0.615827	0.019305	-21.0906627	**2.58516E-89**
mediastinal mass	0.647695	0.034419	**0.709825**	0.031109	42.3483101	**3.0928E-280**
central vascular redistribution	0.354491	0.034431	**0.728932**	0.031302	254.4623065	**0**
vertebral fracture	0.499654	0.02921	**0.791375**	0.015662	278.3320678	**0**
superior mediastinal enlargement	**0.596948**	0.024252	0.551017	0.025206	-41.52441949	**2.9881E-272**
vascular hilar enlargement	0.623934	0.007406	**0.625607**	0.007007	5.189078029	**2.32751E-07**
nodule	**0.546737**	0.010556	0.446317	0.010124	-217.1150565	**0**
air trapping	0.580882	0.006245	0.580408	0.005897	-1.745118047	0.081118057
bullas	0.486494	0.020169	**0.744606**	0.018356	299.2954863	**0**
ground glass pattern	0.602802	0.027608	**0.671321**	0.020656	62.84105487	**0**
calcified adenopathy	0.583562	0.02315	**0.673757**	0.019228	94.77745188	**0**
minor fissure thickening	**0.77315**	0.018481	0.600411	0.025956	-171.4357871	**0**
unchanged	0.395541	0.004386	**0.618171**	0.004502	1120.102208	**0**
clavicle fracture	**0.607514**	0.036746	0.596974	0.037946	-6.309943613	**3.42827E-10**
pseudonodule	**0.557981**	0.009991	0.476977	0.011371	-169.2291715	**0**
end on vessel	**0.560626**	0.035794	0.397635	0.041243	-94.38338959	**0**
COPD signs	**0.751217**	0.003745	0.650859	0.004075	-573.421393	**0**

26

Comparing Unregularized baseline (Ours) to TIER (Ours) on Padchest head-to-head:

Table 11: Two sample t-test for the difference of mean AUCs for our padchest evaluation. In this table, we compare our unregularized and regularized (TIER) models. Each model had AUC evaluated on 1000 bootstraps of the radiologists-labeled subset of padchest. All but the cardiomegaly, emphysema, pneumothorax, and clavicle fracture findings are significant at the p=0.0001 level. TIER wins for 30 findings, achieving an average AUC of 0.755, while the unregularized model wins for 23 findings, achieving a lower average AUC of 0.743.

Label	Unreg. (Ours) Mean	Unreg. Std	TIER (Ours) Mean	TIER Std	T statistic	P value
Average AUC	0.742534	0.002567	**0.75542**	0.002347	117.1556311	**0**
Number won	23		**30**			
endotracheal tube	0.956634	0.008621	**0.979606**	0.005919	69.46676879	**0**
pleural effusion	0.930292	0.003377	**0.942045**	0.002976	82.56984314	**0**
pulmonary edema	**0.945415**	0.008526	0.941289	0.008719	-10.69926209	**5.11898E-26**
heart insufficiency	**0.927177**	0.005282	0.926097	0.005453	-4.498643855	**7.23167E-06**
pulmonary fibrosis	0.944147	0.006584	**0.951654**	0.0054	27.87855697	**9.3138E-145**
cardiomegaly	0.883339	0.002701	0.883692	0.002718	2.913187348	0.00361733
vascular redistribution	0.872019	0.013502	**0.877236**	0.013662	8.588841321	**1.73859E-17**
consolidation	0.849872	0.011331	**0.878342**	0.009453	61.01092612	**0**
hilar congestion	0.850243	0.008691	**0.855435**	0.008915	13.18723777	**3.87838E-38**
pulmonary mass	**0.872299**	0.012346	0.844107	0.012986	-49.75455492	**0**
cavitation	0.794295	0.017229	**0.857639**	0.015601	86.18194266	**0**
alveolar pattern	0.816974	0.006339	**0.87631**	0.005049	231.535272	**0**
calcified pleural thickening	0.84287	0.019733	**0.859651**	0.020362	18.71497205	**3.84423E-72**
lung metastasis	0.860837	0.017219	**0.877375**	0.015578	22.52272401	**2.7303E-100**
emphysema	0.718377	0.013149	0.717841	0.013142	-0.911743481	0.362013758
interstitial pattern	**0.840368**	0.005014	0.835144	0.005382	-22.45845998	**8.6714E-100**
costophrenic angle blunting	**0.808131**	0.00461	0.769921	0.006022	-159.323741	**0**
tuberculosis	**0.843741**	0.024721	0.838961	0.020022	-4.751556022	**2.1624E-06**
atelectasis	**0.791507**	0.0086	0.781707	0.008707	-25.32275656	**6.2416E-123**
reticular interstitial pattern	**0.867637**	0.019332	0.844479	0.022699	-24.56163626	**1.2365E-116**
pneumonia	0.796614	0.005068	**0.813796**	0.004699	78.6172414	**0**
lobar atelectasis	**0.815725**	0.013775	0.808411	0.014991	-11.36063996	**4.99873E-29**
normal	**0.790588**	0.003023	0.776328	0.003632	-95.42795587	**0**
pleural thickening	0.754608	0.016022	**0.784428**	0.014559	43.55866303	**5.5682E-292**
reticulonodular interstitial pattern	0.838374	0.026992	**0.862346**	0.024737	20.70489002	**1.95964E-86**
infiltrates	0.735399	0.006646	**0.742854**	0.006681	25.01662683	**2.1878E-120**
hypoexpansion	**0.871452**	0.010845	0.853423	0.011148	-36.65734018	**1.9617E-225**
hypoexpansion basal	0.874477	0.014044	**0.889652**	0.013677	24.47917337	**5.8658E-116**
humeral fracture	0.672935	0.028067	**0.742305**	0.026582	56.74716788	**0**
pneumothorax	0.728547	0.021418	**0.730643**	0.026112	1.962595625	0.049831759
multiple nodules	**0.852951**	0.020427	0.790815	0.021245	-66.66997483	**0**
hyperinflated lung	0.667704	0.017846	**0.700879**	0.018276	41.06987413	**7.5179E-268**
bronchiectasis	**0.743998**	0.009203	0.734643	0.009854	-21.94072646	**8.91339E-96**
adenopathy	**0.73105**	0.017982	0.678726	0.016664	-67.49145771	**0**
mediastinal enlargement	0.666796	0.028092	**0.72538**	0.026617	47.87154657	**0**
laminar atelectasis	**0.687839**	0.006426	0.67343	0.006914	-48.27281362	**0**
vertebral compression	**0.734413**	0.019904	0.723955	0.018277	-12.2383364	**2.91558E-33**
rib fracture	0.668069	0.023081	**0.689835**	0.022485	21.36070437	**2.38093E-91**
tuberculosis sequelae	0.773832	0.014015	**0.796895**	0.013529	37.44003048	**6.6415E-233**
hilar enlargement	0.714687	0.011757	**0.721779**	0.011469	13.65450364	**1.19318E-40**
tracheal shift	0.500734	0.02327	**0.615827**	0.019305	120.3743682	**0**
mediastinal mass	0.409473	0.031929	**0.709825**	0.031109	213.0621769	**0**
central vascular redistribution	0.567387	0.046306	**0.728932**	0.031302	91.39738689	**0**
vertebral fracture	**0.86009**	0.013028	0.791375	0.015662	-106.6628934	**0**
superior mediastinal enlargement	**0.637878**	0.021595	0.551017	0.025206	-82.75530027	**0**
vascular hilar enlargement	0.60417	0.007237	**0.625607**	0.007007	67.29618289	**0**
nodule	**0.507929**	0.011538	0.446317	0.010124	-126.9283034	**0**
air trapping	**0.631534**	0.005968	0.580408	0.005897	-192.699814	**0**
bullas	0.584846	0.023316	**0.744606**	0.018356	170.2487729	**0**
ground glass pattern	0.661248	0.021925	**0.671321**	0.020656	10.57463045	**1.81468E-25**
calcified adenopathy	0.624151	0.023153	**0.673757**	0.019228	52.12228786	**0**
minor fissure thickening	0.558331	0.022571	**0.600411**	0.025956	38.68594962	**7.5149E-245**
unchanged	**0.633874**	0.004591	0.618171	0.004592	-77.22708382	**0**
clavicle fracture	0.596031	0.041522	0.596974	0.037946	0.530145578	0.596069909
pseudonodule	0.472281	0.010954	**0.476977**	0.011371	9.405369698	**1.37144E-20**
end on vessel	**0.485072**	0.037602	0.397635	0.041243	-49.54199726	**0**
COPD signs	**0.652912**	0.00394	0.650859	0.004075	-11.45351594	**1.83491E-29**